Probing nanoparticle substrate interactions with synchrotron infrared nanospectroscopy: Coupling gold nanorod Fabry-Pérot resonances with SiO_2 and *h*-BN phonons

Joseph J. Liberko,[1] Jacob A. Busche,[2] Robyn Seils,[3] Hans A. Bechtel,[4] Philip D. Rack,[3,5] David J. Masiello,[2,*] and Jon P. Camden[1,†]

[1]*Department of Chemistry and Biochemistry, University of Notre Dame, Notre Dame, Indiana 46556, USA*
[2]*Department of Chemistry, University of Washington, Seattle, Washington 98195, USA*
[3]*Department of Materials Science and Engineering, University of Tennessee, Knoxville, Tennessee 37996, USA*
[4]*Advanced Light Source Division, Lawrence Berkeley National Laboratory, Berkeley, California 94720, USA*
[5]*Center for Nanophase Materials Science, Oak Ridge National Laboratory, Oak Ridge, Tennessee 37831, USA*

(Received 26 February 2021; revised 10 May 2021; accepted 24 June 2021; published 12 July 2021)

Spectroscopic interrogation of materials in the midinfrared with nanometer spatial resolution is inherently difficult due to the long wavelengths involved, reduced detector efficiencies, and limited availability of spectrally bright, coherent light sources. Technological advances are driving techniques that overcome these challenges, enabling material characterization in this relatively unexplored spectral regime. Synchrotron infrared nanospectroscopy (SINS) is an imaging technique that provides local sample information of nanoscale target specimens in an experimental energy window between 330 and 5000 cm^{-1}. Using SINS, we analyzed a series of individual gold nanorods patterned on a SiO_2 substrate and on a flake of hexagonal boron nitride. The SINS spectra reveal interactions between the nanorod photonic Fabry-Pérot resonances and the surface phonon polaritons of each substrate, which are characterized as avoided crossings. A coupled oscillator model of the hybrid system provides a deeper understanding of the coupling and provides a theoretical framework for future exploration.

DOI: 10.1103/PhysRevB.104.035412

I. INTRODUCTION

Advances in the design of nanoengineered materials endowed with tailorable mid-infrared (IR) responses have been accelerated by decades of prior research in plasmonics, photonics, and phononics. By leveraging knowledge gained from these communities, new strategies for creating tunable light-matter states that operate across the IR have emerged based on hybridizing electronic, optical, and vibrational degrees of freedom [1–3]. In such materials, their composite responses find origin in their bulk dielectric properties together with particle morphology and cluster geometry [4–9]. Characterizing these properties with simultaneously high spatial and spectral resolution is difficult but essential for the rational design of advanced materials with novel functionalities [10–14]. Today, a number of studies have made progress in this direction through a variety of near-field imaging and spectroscopy techniques [15–23], yet considerable work still lies ahead to better understand material design principles and characterization methods in the IR spectral regime.

In this work, we investigate the nanoscale resonant coupling between the mid-IR Fabry-Pérot (FP) modes of high-aspect ratio noble-metal nanorods [24–29] with the surface-phonon polaritons (SPhPs) [30,31] of their supporting substrates. Due to their lightlike nature, we will refer to these surface plasmon polaritons as Fabry-Pérot (FP) modes [24]. Previous work by Huck *et al.* [32] measured far-field extinction spectra from gold nanorods on SiO_2 substrates of various thicknesses and discovered an avoided crossing when the resonance positions of the nanorod series were plotted versus inverse nanorod length; however, these measurements did not probe the coupling in the near field. More recently, Tizei *et al.* [33] explored strong coupling between SPhPs and the first FP mode in long metal nanowires using electron energy-loss spectroscopy (EELS) performed in a scanning transmission electron microscope (STEM). In this study, silver nanorods were placed on thin hexagonal boron nitride (hBN) flakes with their ends suspended off the substrate. Probing the vacuum end of the nanorod minimized substrate losses and allowed the nanorod length to be systematically milled, via the electron beam, to tune the FP response and produce an avoided crossing in the EEL spectrum. In general, the presence or absence of an avoided crossing depends on the specifics of the nanoparticle-substrate system and an avoided crossing is not expected when dealing with lossy modes or weak coupling [34]. The facile tunability of the nanorod FP resonances employed here makes it an ideal system to study particle-substrate coupling.

Scattering-type scanning near-field optical microscopy (s-SNOM) utilizes light that is coupled into an atomic force microscope (AFM) to create a region of concentrated surface charges induced at its tip. The scattered field of these charges subsequently interacts with a target material, simultaneously gathering information about the spatial and spectral profiles of the target's optical modes [35–40]. Since the scattered field contains both radiative and nonradiative components, the

*masiello@uw.edu
†jon.camden@nd.edu

selection rules for s-SNOM are relaxed compared to far-field plane-wave illumination, as the actual collected signal in s-SNOM is the radiation from the coupled tip-sample region. Direct measurement of a nanoparticle's dielectric response using such techniques provides (1) a window into resonant energy transfer between nanostructured materials with their supporting substrates, (2) a method for analyzing irregularities of thin-film structures, and (3) an avenue for exploring quantum-size and surface-scattering effects [41–44]. Additionally, because the tip's characteristic length scale is on the order of tens of nanometers, near-field effects allow s-SNOM to overcome Abbe's diffraction limit [45].

By design, s-SNOM relies on a spectrally bright, collimated, and coherent light source because the tip focusing and scattering processes are inefficient. While this limitation has largely been overcome in the optical and ultraviolet spectral regions by advancements in laser technology, highly tunable IR sources remain limited [36]. Recently, Bechtel and co-workers [46] implemented an s-SNOM variant using the broadband and high-intensity IR radiation available from the synchrotron at the Advanced Light Source (ALS) at Lawrence Berkeley National Laboratory called synchrotron infrared nanospectroscopy (SINS); see Fig. 1. The rich IR spectral content of the ALS allows the response of a sample to be simultaneously collected at all IR frequencies to which available photon detectors are sensitive. The current ALS SINS instrument system is capable of ∼0.5 meV spectral resolution that is considerably better than the ∼5 meV resolution of STEM EELS such that, taken together with the 25 nm spatial resolution provided by the AFM tip, SINS is a uniquely powerful technique with which to probe nanostructures, especially those with narrow resonances, in the mid-IR region [47–56].

We begin by presenting SINS data to explore the transfer of energy between the low-energy multipolar FP modes of individual gold nanowires and the IR SPhPs in a polar crystal substrate. Nanorod lengths are systematically fabricated and measured to evolve these FP modes through the highest energy SPhP substrate mode of SiO_2. Next, the substrate is exchanged for a van der Waals material to explore how the nanowire FP modes interact with a different inherent set of IR SPhPs. To gain physical insight, we model the system analytically, deriving the SINS signal from the tip's effective polarizability and interpreting the spectral features contained therein with a simple oscillator model.

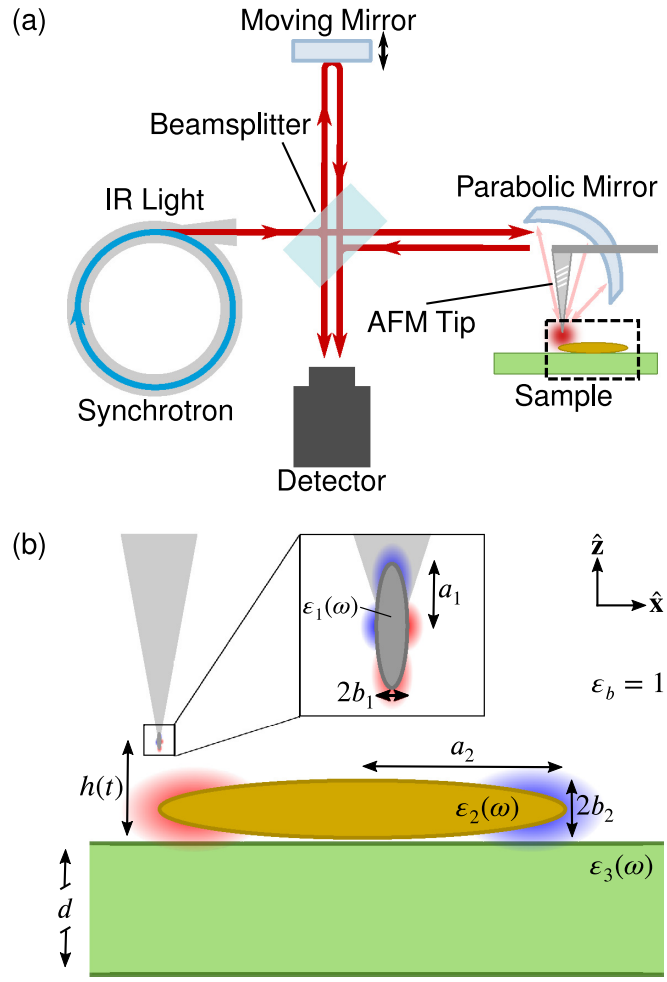

FIG. 1. (a) Schematic of the experimental SINS setup. The dashed box encloses the tip-sample interaction region. (b) Geometry of the idealized sample system and the model parameters used to build an analytical oscillator model of the tip-sample interaction (see text for details).

II. RESULTS AND DISCUSSION

A. Individual nanorod analysis

The second harmonic SINS response of two nanorods (1.13 μm and 2.18 μm) on SiO_2 are shown in Fig. 2 as a function of scan distance along the centerline of each nanorod. SINS of the bare SiO_2 substrate [Fig. S1 of the Supplemental Material (SM) [57]] reveals a SPhP at 1219 cm^{-1} in the phase spectrum and at 1126 cm^{-1} in the magnitude spectrum. Interestingly, this substrate feature is able to be detected through the 30 nm thick gold nanorod as seen in the SINS phase and magnitude spectra of the 1.13 μm nanorod along its full length. Lobes are observed at both nanorod ends around 2500 cm^{-1} in the SINS phase spectra and around 2200 cm^{-1} in the magnitude spectra [Figs. 2(a) and 2(b)]. The spatial distribution and energy range of this feature, together with previous studies [12,24,58], indicates that this is the first, $m = 1$, FP mode. As the nanorod's first FP mode and substrate's SPhP are separated by ∼1200 cm^{-1}, little mixing is expected.

Increasing the nanorod length shifts the $m = 1$ FP feature toward the lower energy SiO_2 SPhP [24], promoting interactions between the nanorod and substrate. SINS phase and magnitude line scan spectra of a 2.18 μm nanorod are shown in Figs. 2(c) and 2(d), where the $m = 1$ FP mode energy approaches the SPhP and a splitting is observed on either side of the SiO_2 phonon, with peaks at 950 cm^{-1} and 1450 cm^{-1} in both SINS phase and magnitude. Lengthening the nanorod also introduces a new feature in both spectra (around 2700 cm^{-1} in the phase spectra), which we attribute primarily to the second, $m = 2$, FP mode based upon strong localization at the center of the nanorod. To further explore the peak splitting attributed to the first two FP modes and SPhP mixing, we performed additional SINS characterization on more than two dozen nanorods of varying length on both SiO_2 and hBN substrates.

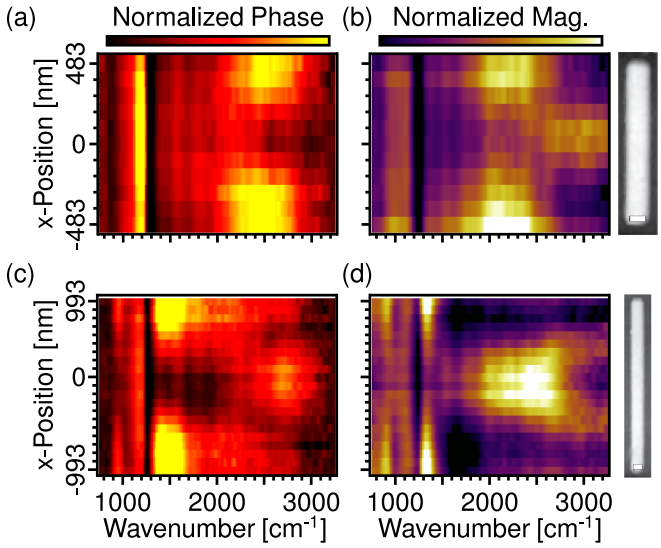

FIG. 2. SINS line scans showing the normalized phase [(a) and (c)] and normalized magnitude [(b) and (d)] for 1.13 [(a) and (b)] and 2.18 [(c) and (d)] μm long nanorods on an SiO_2 substrate as a function of distance from the nanorod center. AFM images of the nanorods scanned are included on the right, with each horizontal scale bar representing 100 nm. The unmixed $m = 1$ FP mode is observed in the shorter nanorod, whereas the longer nanorod shows the mixing of the $m = 1$ FP mode with the substrate phonon and the emergence of the unmixed $m = 2$ FP mode. To better highlight these behaviors, SINS intensity information is displayed over a given range (0.1–0.7 rad and 0.4–1.0 V) so that data outside of it saturates the image.

B. Complete nanorod series analysis

A series of Au nanowires ($L = 0.7$–10.0 μm; details in Table SI of the SM) were lithographically patterned onto two different substrates: (1) 100 nm thick amorphous SiO_2 on a Si wafer and (2) 330 nm thick flake of exfoliated hBN on a Si wafer. Measurements were performed at the tip and center of each nanorod in the series to track the $m = 1$ and $m = 2$ FP modes, respectively. The second harmonic SINS magnitude components are reported in Fig. 3 (phase is reported in Fig. S3 of the SM), where the top of each waterfall plot begins with the shortest nanorod and ends at the bottom with the longest nanorod. For the SINS magnitude measurements obtained at the tip of the shortest nanorods (top traces of Fig. 3) the SPhP feature is clearly isolated at 1126 and 1389 cm^{-1} for SiO_2 and hBN, respectively, with only the beginning of the red shoulder from the $m = 1$ FP mode appearing in the high energy region. We confirm this as a SPhP feature by performing SINS on each substrate, in the absence of nanorods, to isolate and identify the substrate phonons (see Figs. S1 and S2 of the SM). SINS performed at the center of the shortest nanorods (top red traces in Fig. 3) also exhibit an isolated SPhP feature.

Increasing the nanorod length allows the FP modes [24] to mix with the SPhP, causing a secondary peak to emerge at 987 cm^{-1} in SiO_2 and at 1296 cm^{-1} in hBN. Interestingly, these secondary peaks emerge asymptotically, shifting to lower energies. While the secondary peaks on the SiO_2 substrate quickly diverge out of the observation window, the secondary peaks on hBN appear to converge towards 849 cm^{-1}. Concurrently, the FP peak redshifts and asymptotes on the high energy side of the SPhP. This peak splitting around the isolated SPhP energy is indicative of an avoided crossing and further insight is provided by plotting the peak positions of both modes versus inverse nanorod length for each substrate (Fig. 4).

Figure 4 displays the avoided crossings between the substrate SPhPs and the nanorod $m = 1$ (blue) and $m = 2$ (red) FP modes as measured in SINS magnitude (the associated avoided crossing in phase is presented in the SM as Fig. S3). In the SiO_2 avoided crossing, the asymptotic energies are 1248 cm^{-1} for the upper branch and 987 cm^{-1} for the lower branch. For the substrate thickness probed here, the upper branch of the avoided crossing is expected to align with the substrate's longitudinal optical phonon (LO) energy, while the lower branch should align with the transverse optical phonon (TO) [32]. Our results are in good agreement with the previously reported LO and TO energies in amorphous SiO_2 (1248 cm^{-1} and 1064 cm^{-1}, respectively) [30], and are further consistent with the previously described far-field extinction measurements of a similar system [32].

Analyzing the nanorod evolution on hBN yields asymptotic energies of 1527 cm^{-1} for the upper branch and 1296 cm^{-1} for the lower branch of the avoided crossing. The branch energies observed here are in good agreement with previous measurements of the LO and TO in hBN [59]. In a similar experiment, Ag nanorods on thinner flakes of hBN were investigated using EELS to reveal an avoided crossing [33], although the mixing of the $m = 2$ FP mode with the SPhP was not fully observed. Nevertheless, the avoided crossing in Fig. 3 clearly indicates the mixing of the $m = 1$ and $m = 2$ FP modes of Au nanorods with SPhPs in hBN. In addition, the upper branch of a second avoided crossing in hBN is evidenced by a concavity change around 1050 cm^{-1} in the lower $m = 1$ branch and energies asymptotically approaching 849 cm^{-1} for the lowest values of inverse nanorod length. The latter energy aligns well with the next highest LO present in hBN, which has a recorded value of 828 cm^{-1} [59]. The forbidden region in the avoided crossings is the spectral range between the upper and lower branches and has a maximum value determined by the energy separation of a substrate's LO and TO values. Known as the Reststrahlen band, this spectral region is most often where $\mathrm{Re}(\varepsilon)$ is negative [60]. In our experiments, we find branch separation energies of 261 cm^{-1} and 231 cm^{-1} for the SiO_2 and hBN substrates, respectively. These results are in good agreement with the expected Reststrahlen bands calculated from their previously reported LO and TO values [30,59]. Interestingly, these values correspond to roughly half of the minimum separation energies between the upper and lower peak position of both FP nanorod resonances on each substrate; see Table S2 of SM.

C. Modeling and discussion

1. Reconstruction of the SINS observable

To augment the interpretation of the SINS signal, we present a reduced-order analytical model of the interactions between a FP mode of the Au nanorod and a SPhP of the substrate. The model provides a simple and intuitive picture of the electromagnetic interactions within the sample and

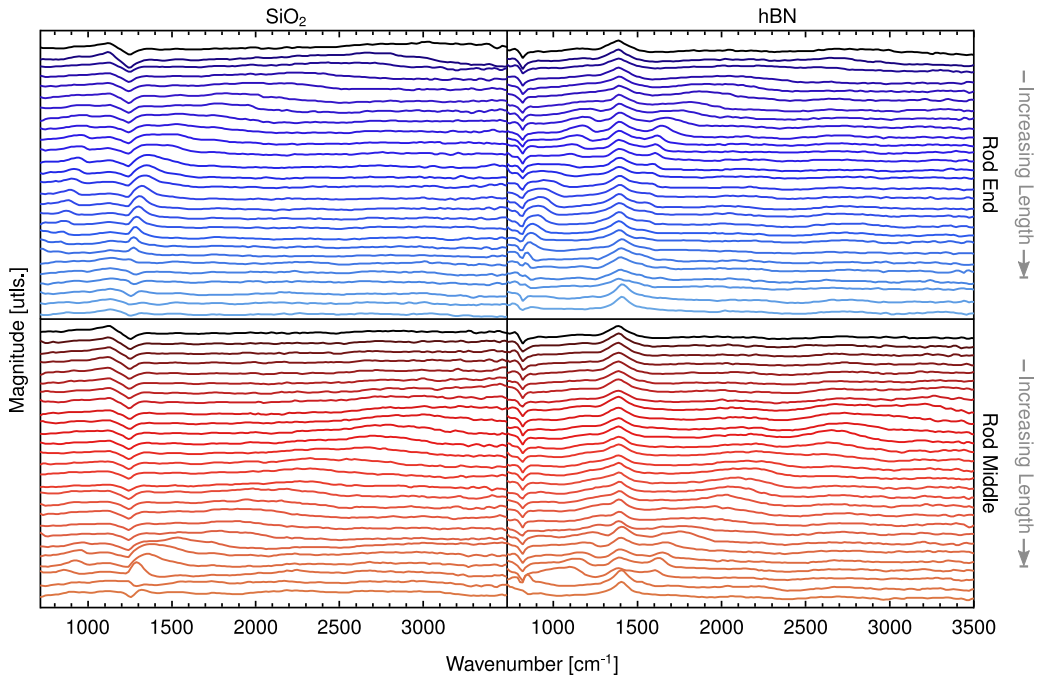

FIG. 3. SINS magnitude spectra from a series of nanorods ($L = 0.7$–$10.0\ \mu$m) obtained at the end (blue tones) or middle (red tones) of the nanorod on SiO_2 (first column) and hBN (second column) substrates. The spectrum obtained from the shortest nanorod is plotted at the top in each panel with longer nanorod spectra vertically offset until the longest nanorod in each series is plotted at the bottom.

how each contributes to the observed spectra. As quantitative calculations involving the resonant surface modes of large particles are mathematically complicated and computationally expensive, we substitute these phenomena with simpler resonances that qualitatively reproduce the behavior of the system.

The $m = 1$ FP mode of the target nanorod is modeled as the nonradiative long-axis dipolar mode of a prolate spheroid with long-axis radius a_2 and short-axis radius b_2; see Fig. 1. The long axis is taken to lie along the x axis and the short axes lie in the yz plane. The spectral properties of the dipolar mode

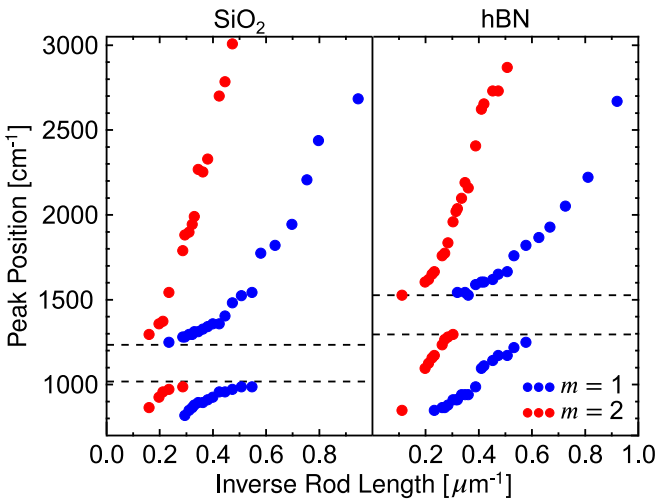

FIG. 4. Avoided crossing diagram derived from the SINS magnitude measurements for the complete nanorod series on both SiO_2 and hBN substrates. The $m = 1$ (blue) and $m = 2$ (red) FP modes are plotted versus inverse nanorod length. Dotted black lines are the asymptotic energies.

are recovered from its polarizability, $\alpha_2(\omega)$, which encodes the contributions of both the nanorod's dielectric function $\varepsilon_2(\omega)$ and geometry and allows the dipolar mode to be approximated as a point dipole located at the spheroid's center [57,61]. The dipole is defined as $\mathbf{p}_2(\omega) = \alpha_2(\omega)\boldsymbol{\mathcal{E}}_{2x}(\mathbf{0}, \omega)$, wherein $\mathbf{p}_2(\omega)$ is the nanorod's long-axis dipole moment and $\boldsymbol{\mathcal{E}}_{2x}(\mathbf{r}, \omega)$ is the x component of the total electric field $\boldsymbol{\mathcal{E}}_2(\mathbf{r}, \omega)$ that impinges on the nanorod.

The coupling between the nanorod and its surroundings is provided through this total field. It can be expanded as $\boldsymbol{\mathcal{E}}_2(\mathbf{r}, \omega) = \mathbf{E}_0(\omega) + \mathbf{E}_1(\mathbf{r}, \omega) + \mathbf{E}_3(\mathbf{r}, \omega)$, where $\mathbf{E}_0(\omega)$ is the electric field provided by the synchrotron light source, assumed here to be spatially uniform within the tip-sample region and linearly polarized with components along both the x and z axes. Further, $\mathbf{E}_1(\mathbf{r}, \omega)$ is the field scattered from the AFM tip and $\mathbf{E}_3(\mathbf{r}, \omega)$ is the field scattered from the substrate. The last field can be modeled as the image response of the substrate to the excitation provided by the synchrotron, tip, and target, and is proportional to the surface response function $\beta(\omega) = [\varepsilon_3(\omega) - 1]/[\varepsilon_3(\omega) + 1]$, with $\varepsilon_3(\omega)$ representing the substrate's dielectric function.

The tip's scattered field is modeled as originating from a superposition of two dipoles, one oriented parallel to the surface of the substrate and the other normal, that lie at the centroid of the tip, $\mathbf{r}_1$. The tip is taken to be a z-oriented prolate spheroid of long-axis radius a_1, short-axis radius b_1, and dielectric $\varepsilon_1(\omega)$ with a centroid raised a height $h > a_1$ above the substrate (see Fig. 1), such that the substrate-normal dipole is oriented along the tip's long axis, and the substrate-parallel dipole along the short axis. Similar to the treatment of the target nanorod, the tip's long (l) and short (s) axis dipole modes are given the polarizabilities of their spheroidal counterparts, $\mathbf{p}_1^{l,s}(\omega) = \alpha_1^{l,s}(\omega)\boldsymbol{\mathcal{E}}_{1z,1x}(\mathbf{r}_1, \omega)$ [see Eq. (A16) of

the SM], with $\boldsymbol{\mathcal{E}}_{1i}(\mathbf{r},\omega)$ the ith component of the total electric field $\boldsymbol{\mathcal{E}}_1(\mathbf{r},\omega)=\mathbf{E}_0(\omega)+\mathbf{E}_2(\mathbf{r},\omega)+\mathbf{E}_3(\mathbf{r},\omega)$ acting on the tip. A more detailed discussion of these approximations is given further on.

The complete spectral response of the tip is especially useful, as it encodes the observable SINS spectrum. The most convenient way to describe this response is through the effective polarizabilities $\hat{\alpha}_1^{l,s}(\omega)$. These polarizabilities encapsulate the influence of all external sources on $\mathbf{p}_1^{l,s}(\omega)$, including sources which are in turn influenced by $\mathbf{p}_1^{l,s}(\omega)$ through coupling forces [62]. In this way, only a single force of the many that dictate the tip's polarization needs to be tracked, and the details of the rest of the system's motion follow from $\hat{\alpha}_1^{l,s}(\omega)$. In general, the only source of the tip's polarization that is experimentally characterizable is the synchrotron light, so it is singled out in the implicit definition $\mathbf{p}_1^{l,s}(\omega)=\hat{\alpha}_1^{l,s}(\omega)\mathbf{E}_{0z,0x}(\omega)$, wherein $\mathbf{E}_{0i}(\omega)$ is the ith component of the synchrotron field. Thus, with knowledge of the explicit forms of the effective polarizabilities and the synchrotron field, the magnitude and phase of the tip's dipole moment and associated scattered fields can be recovered and converted, through oscillation of the tip and lock-in detection, into the SINS observable [see Eq. (3)].

The derivations of $\hat{\alpha}_1^{l,s}(\omega)$ are lengthy (see SM) but result in

$$\hat{\alpha}_1^{l}(\omega)=\alpha_1^{l}(\omega)\frac{1+\beta(\omega)}{1-\alpha_1^{l}(\omega)\beta(\omega)/4h^3},$$

$$\hat{\alpha}_1^{s}(\omega)=\alpha_1^{s}(\omega)\frac{1+2\hat{\alpha}_2(\omega)/\left(a_2^2+[h-b_2]^2\right)^{\frac{3}{2}}}{1-\alpha_1^{s}(\omega)\beta(\omega)/8h^3+4\alpha_1^{s}(\omega)\hat{\alpha}_2(\omega)/\left(a_2^2+[h-b_2]^2\right)^{3}}. \tag{1}$$

For both tip dipoles, the effective polarizability is the product of its free-space polarizability $\alpha_1^{l,s}(\omega)$ and a frequency-dependent dressing factor. In the limit both $\hat{\alpha}_2(\omega)$ and $\beta(\omega)$ go to zero, either factor goes to one, and the effective polarizabilities return to their free-space values. Further,

$$\hat{\alpha}_2(\omega)=\alpha_2(\omega)\frac{1}{1-\alpha_2(\omega)\beta(\omega)/8b_2^3} \tag{2}$$

is the nanorod dipole's effective polarizability. Note that Eq. (2) does not depend on either polarizability $\alpha_1^{l,s}(\omega)$ of the tip, such that the nanorod's spectral response is assumed to be altered only by the substrate. This approximation is valid here because the tip's long-axis dipole cannot couple to the target nanorod's dipolar mode at all by symmetry and the tip's short-axis dipole (which can couple) is both far detuned from the nanorod's response and many orders of magnitude weaker. More specifically, the detuning between the maxima of $\mathrm{Im}\,\alpha_1^{s}(\omega)$ and $\mathrm{Im}\,\alpha_2(\omega)$ is roughly $70\gamma_2$, with γ_2 the nanorod mode's FWHM, and the ratio of the maxima is $\sim 10^{-5}$.

The substrate's modification of the nanorod's response is contained in the second term in the denominator of $\hat{\alpha}_2(\omega)$, which indicates coupling between the dipole and resonances in the substrate. In the case where $\alpha_2(\omega)$ and $\beta(\omega)$ each have a sufficiently strong single resonance, this term leads to mode splitting, as can be checked by comparison to the spectrum of two coupled oscillators [57].

Each of the terms in the dressing factors of $\hat{\alpha}_1^{l,s}(\omega)$ are similarly responsible for encoding coupling effects into the tip's response. The numerator of either factor builds in additional driving forces on the tip that arise as the synchrotron directly excites the substrate (in $\hat{\alpha}_1^{l}$) or target (in $\hat{\alpha}_1^{s}$) and causes surface charges in either to push back on the tip. Meanwhile, the denominators encode coupling effects: the terms that go like $\alpha_1^{l,s}(\omega)\beta(\omega)/h^3$ describe tip-substrate coupling and the term in $\hat{\alpha}_1^{s}$'s denominator proportional to $\alpha_1^{s}(\omega)\hat{\alpha}_2(\omega)$ builds tip-target coupling into the tip's response. From these terms, one can conclude that only the short-axis dipole of the tip can couple to $\mathbf{p}_2(\omega)$. The long-axis dipole can only couple to the substrate, such that the observables of $\mathbf{p}_1^{l}(\omega)$ serve only to obscure the features of $\hat{\alpha}_1^{s}(\omega)$.

Translation of the effective polarizabilities of the tip to a SINS signal is performed by allowing the tip-substrate separation to become time dependent, such that $h\rightarrow h(t)=h_0+\Delta h\cos(\Omega_0 t)$, where h_0 is the time-average separation, Δh is the modulation depth, and $\Omega_0\sim 100\,\mathrm{kHz}$ is the tip's oscillation frequency. The resulting time-dependent polarizabilities $\hat{\alpha}_1^{l,s}(\omega)$ can be expanded into a Fourier series with complex coefficients

$$A_n^{l,s}(\omega)=\frac{\Omega_0}{2\pi}\int_{-\frac{\pi}{\Omega_0}}^{\frac{\pi}{\Omega_0}}\hat{\alpha}_1^{l,s}(\omega,t)e^{ni\Omega_0 t}dt, \tag{3}$$

which are known to reproduce both the magnitude and phase of the SINS signal up to a scaling factor [38]. The synchrotron's light is assumed to be polarized at 45° to the x axis, such that both the long- and short-axis dipole modes of the tip are driven equally. The second-order Fourier coefficient of the total field flux at the location of the detector is then proportional to the average of the coefficients of the fields from each tip dipole, and can be modeled up to a constant scale factor by $A_2(\omega)=[A_2^{l}(\omega)+A_2^{s}(\omega)]/2$.

Figure 5 shows the absolute magnitude $|A_2(\omega)|$. The tip is made of PtSi, which in the range of energies considered in Fig. 5 is well modeled by a Drude-model dielectric $\varepsilon_1(\omega)=1-\omega_{p1}^2/(\omega^2+i\omega\gamma_1)$ with plasma wave number $\omega_{p1}/2\pi c=2.98\times 10^4\ \mathrm{cm}^{-1}$ and damping wave number $\gamma_1/2\pi c=645\ \mathrm{cm}^{-1}$ [66]. The metallic motion of the tip's electrons as well as its micron-scale length and conical geometry likely impart on it an optical response dominated by a continuous spectrum of propagating surface plasmon modes. While the existence and properties of these modes have not yet been experimentally explored in PtSi tips, they have recently been investigated in similarly conductive gold tips [67–69]. We take from these earlier studies two conclusions, namely that the

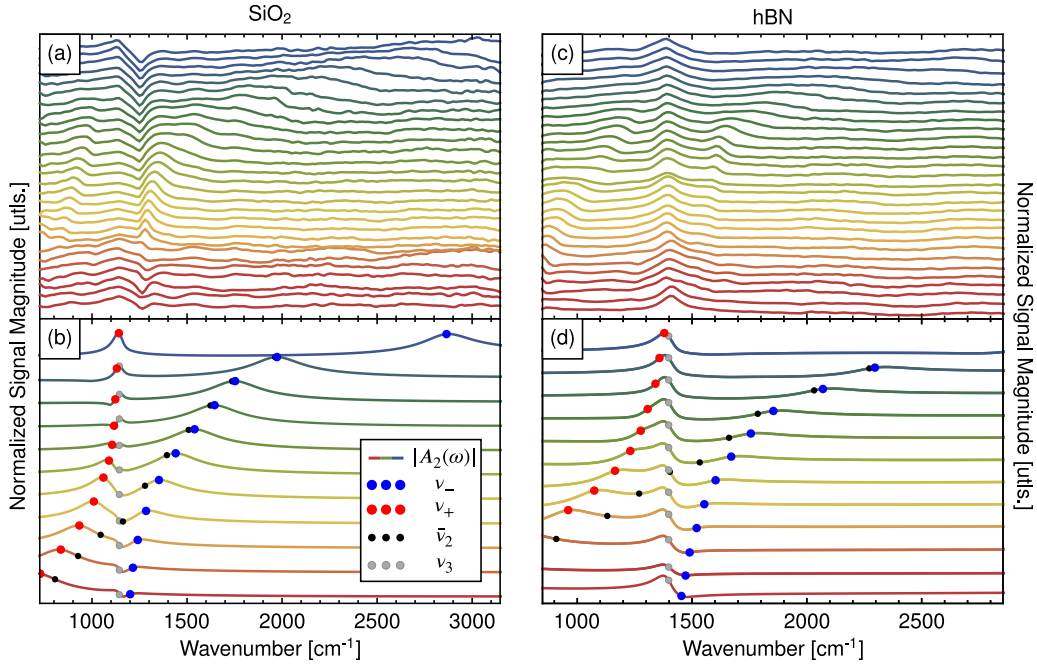

FIG. 5. Comparison of experimentally collected [(a), (c)] and theoretically constructed [(b), (d)] SINS magnitude spectra $|A_2(\omega)|$ of the $m = 1$ nanorod FP mode. The experimental spectra were obtained from a series of target gold nanorods of lengths varying from $L = 0.7$ to 10.0 μm, while the theoretical spectra were generated using a target spheroid of long axis radius $a_2 = 9$ μm, short-axis radius $b_2 = 550$ nm, plasma wave number $\omega_{p2}/2\pi c = 1633$ cm^{-1}, scattering wave number $\gamma_2/2\pi c = 256.5$ cm^{-1}, and variable Lorentz wave number $\omega_2/2\pi c =$ 805.5–2977 cm^{-1}. The nanorods were mounted on SiO_2 (a) and hBN (c) substrates, and these substrates were modeled theoretically [(b), (d)] with plasma wave numbers $\omega_{p3}/2\pi c = 362.9$ and 1169 cm^{-1}, damping wave numbers $\gamma_3/2\pi c = 64.12$ and 92.75 cm^{-1}, Lorentz wave numbers $\omega_3/2\pi c = 1147$ and 1398 cm^{-1}, and intraband dielectric constants $\varepsilon_{\infty 3} = 1.2$ and 2.68, respectively [63–65]. Additionally, the spectral locations of the uncoupled nanorod dipole ($\bar{\nu}_2$), uncoupled substrate SPhP (ν_3), and hybridized modes ($\nu_\pm$) are superimposed on the spectra to demonstrate the effects of the nanorod-substrate coupling on the observable signal.

electric response of the tip does not contain resonances in the mid-IR when driven by sources near its apex and that the field profiles of its low-energy response are dipolar at each driving frequency ω just below its apex.

Building on previous successes modeling AFM tips using point dipoles and/or spheroidal particles, we model the tip's apex as a pair of point dipoles $\mathbf{p}_1^{l,s}$ with spheroidal polarizabilities that reproduce the apex's featureless low-energy spectral response and field profile [37,38,70]. Both properties are achieved naturally. The spheroid model assumes the tip's response is dominated by a pair of localized surface plasmon dipoles, both of which resonate at energies far higher than the resonance frequencies of the target nanorod dipoles and substrate SPhPs due to the relatively large value of ω_{p1}. Thus the low-energy tails of the resonances provide the tip a flat spectral response below 4000 cm^{-1} (see Fig. S6) that minimally modifies the responses of the nanorod and substrate. The dipolar field profile of the tip immediately emerges from the dipole model.

The target nanorod is given a Lorentz-model dielectric function $\varepsilon_2(\omega) = 1 + \omega_{p2}^2/(\omega_2^2 - \omega^2 - i\omega\gamma_2)$, which provides $\mathbf{p}_2$ a singly peaked resonant spectrum. Although the experiment uses a Au nanorod that is better modeled with a Drude dielectric function, we choose a Lorentz model to easily tune the nanorod's resonance frequency Ω_2 and mimic the hitherto ignored redshift brought on by radiation damping [57]. Explicitly, $\Omega_2 = \sqrt{\omega_2^2 + \omega_{p2}^2 A_{10}(X_2)/[A_{10}(X_2) - B_{10}(X_2)]}$, such that ω_2 can be altered to tune the nanorod's resonance; a Drude model with $\omega_2 \to 0$ is not flexible enough to recreate the magnitude of the radiation-induced shifts. Further, adjustments to the oscillator strength ω_{p2}^2 and damping rate γ_2 allow us to account for the related resonance suppression and linewidth modifications that appear in a fully retarded treatment [24]. Each of the parameters of $\varepsilon_2(\omega)$ was fit to the experimental data and corroborated with gold nanorod data collected from Refs. [24,58].

The substrate's dielectric is simplified, in both Figs. 5(b) and 5(d), to a Lorentz dielectric with a single phonon mode at the LO phonon frequency ω_3 with oscillator strength ω_{p3}^2, damping rate γ_3, and static contribution $\varepsilon_{\infty 3}$, such that $\varepsilon_3(\omega) = \varepsilon_{\infty 3} + \omega_{p3}^2/(\omega_3^2 - \omega^2 - i\omega\gamma_3)$. This simplification allows for a clear depiction of mixing between the dipole's resonance at Ω_2 and the substrate's lone SPhP at $\Omega_3 = \sqrt{\omega_3^2 + \omega_{p3}^2/(\varepsilon_{\infty 3} + 1)}$ at the expense of neglecting the width of the Reststrahlen band of either substrate, within which many SPhPs exist and clear identification of individual hybrid modes is very difficult [30,57,59,60].

The only significant error brought on by this approximation appears near the extremes of the nanorod series, where one pair of hybrid mode energies asymptotes to the edges of the Restrahlen band in the experiment (Fig. 4) and to Ω_3 in the theoretical reproduction. Because the Reststrahlen band of either substrate is narrower than the linewidth of the nanorod's

dipolar mode and largely obscured by a strong peak in each collected spectrum, the vast majority of the observable features in the experimental signal lie outside this region and are well modeled by the single-phonon approximation.

In particular, with an hBN substrate [Figs. 5(c) and 5(d)] the single-phonon approximation reproduces the spectral shifts and avoided crossing of the two peaks observed clearly in the experimental data on either side of the SPhP energy. It also reveals that the observed peaks reach a minimum separation at $|\Omega_2^2 - \Omega_3^2| = 0$, as expected from hybridization theory, and that the dipole's linewidth is reduced due to its mixing with the narrower SPhP.

2. Oscillator model of the nanorod and substrate resonances

In the case of the SiO_2 substrate this behavior is not so clear. The ever-present feature at the SPhP energy, caused by coupling between $\mathbf{p}_1^l(\omega)$ and the SPhP, is altered at many values of Ω_2. This is contrary to the behavior of hBN and produces asymmetries in the line shapes of the hybridized modes. While the effective polarizability model reproduces this behavior and reveals its cause to be the relatively weak phonon oscillator strength of SiO_2, it alone cannot help us to extract the resonance positions of the two hybrid modes from the atypical spectrum with significantly greater certainty than the approximations used to generate Fig. 4 already provide. Instead, the hybridized modes can be extracted with the aid of an oscillator model of the system because it provides analytical expressions for the hybrid resonance frequencies $\Omega_\pm$ via standard mode-mixing techniques. We begin with the definition of a coordinate $x(\omega) = \mathbf{p}_2(\omega)\cdot\hat{\mathbf{x}}/e$, which represents the complex magnitude of $\mathbf{p}_2(\omega)$ and is

$$x(\omega) = \frac{F(\omega)}{m_2}\frac{1}{\Omega_2^2 - \omega^2 - i\omega\gamma_2}. \tag{4}$$

Here, $F(\omega) = e\mathcal{E}_{2x}(\mathbf{0},\omega)$ is the external force acting on the oscillator (assumed to be located at the origin, $\mathbf{r} = \mathbf{0}$) and $m_2 = 3\,e^2(A_{10} - B_{10})/c_2^3\omega_{p2}^2$ is the oscillator's mass.

While the connection between $\mathbf{p}_2(\omega)$ and $x(\omega)$ is straightforward, the connection between the substrate's SPhP and an oscillator coordinate is not. Leaving the details for the SM, the substrate's scattered field at the origin can be defined as

$$\mathbf{E}_3(\mathbf{0},\omega) = -\frac{e}{\sqrt{8L^3b_2^3}}\{[Q_{01}(\omega) + Y_{01}(\omega)]\hat{\mathbf{x}} + [Q_{00}(\omega) + Y_{00}(\omega)]\hat{\mathbf{z}}\}. \tag{5}$$

Here, the coordinates $Q_{pm}(\omega)$ represent independent SPhPs with azimuthal node structure $m = \{0, 1, \ldots\}$ and reflection parity about the x axis (p even or odd). Their resonant behavior is similar to that of $x(\omega)$, with

$$Q_{pm}(\omega) = \frac{\mathcal{F}_{pm}(\omega)}{M_m}\frac{1}{\Omega_3^2 - \omega^2 - i\omega\gamma_3}, \tag{6}$$

wherein $M_m = (2 - \delta_{m0})e^2(\varepsilon_{\infty 3} + 1)^2/\omega_{p3}^2 d^3$ are the mode masses. Due to the substrate's infinite extent, a characteristic length factor, d, is used, akin to the quantization lengths often used in quantum optical theories. As is true in box quantization, the observables of the system are independent of d, and it serves only to provide sensible units and an overall scale to the oscillator picture.

From the forms of Eqs. (5) and (6), it is clear why both dipoles of the tip can couple to an SPhP resonance at Ω_3 in the substrate without indirectly coupling to each other. Because the SPhP responses $1/(\Omega_3^2 - \omega^2 - i\omega\gamma_3)$ are the same for all (p, m) and the tip-substrate couplings are $-\mathbf{p}_1^l(\omega)\cdot\mathbf{E}_{3z}(\mathbf{0},\omega) \propto x(\omega)Q_{00}(\omega)$ and $-\mathbf{p}_1^s(\omega)\cdot\mathbf{E}_{3x}(\mathbf{0},\omega) \propto x(\omega)Q_{01}(\omega)$, the dipoles interact with independent SPhP modes $Q_{pm}(\omega)$ of different symmetry but identical spectral behavior.

The coordinates $Y_{pm}(\omega)$ describe the excitation of independent substrate modes that respond instantaneously to stimuli and do not oscillate. From their definition $Y_{pm}(\omega) = L^3\beta_\infty\mathcal{F}_{pm}(\omega)/(2 - \delta_{m0})e^2$, one can see that as $\varepsilon_{\infty 3} \to 1$ the factor $\beta_\infty = (\varepsilon_{\infty 3} - 1)/(\varepsilon_{\infty 3} + 1) \to 0$. Thus the static coordinates do not contribute to the scattered field unless $\varepsilon_{\infty 3} > 1$.

The functional forms of the forces $\mathcal{F}_{pm}(\omega)$ on the SPhPs are complicated. Derivations of the forces are left for the SM, where their dependence upon the charge distribution of the nanorod and the nanorod coordinate are made explicit. Further, since the force $F(\omega)$ acting on the nanorod dipole contains a term $e\mathbf{E}_3(\mathbf{0},\omega)\cdot\hat{\mathbf{x}}$, we note that $F(\omega) \propto Q_{01}(\omega)$. In this way, the forces on either oscillator mediate their coupling and the forces' explicit forms lead to the coupled equations of motion

$$\begin{aligned} x(\omega)\big(\bar{\Omega}_2^2 - \omega^2 - i\omega\gamma_2\big) - \frac{g}{m_2}Q_{01}(\omega) &= \frac{F_0(\omega)}{m_2}, \\ Q_{01}(\omega)\big(\Omega_3^2 - \omega^2 - i\omega\gamma_3\big) - \frac{g}{m_3}x(\omega) &= 0. \end{aligned} \tag{7}$$

Here, $m_3 = M_1$ is the mass of the lone SPhP mode $Q_{01}(\omega)$ that can couple to the target nanorod's resonance and $F_0(\omega) = eE_{0x}(\omega)$ is the force applied on the nanorod by the synchrotron light. The lowered frequency $\bar{\Omega}_2 = \sqrt{\Omega_2^2 - \beta_\infty e^2/8b_2^3 m_2}$ encapsulates the contribution of $Y_{01}(\omega)$ on the nanorod's spectrum: the substrate's static response induces a redshift on the nanorod's dipole that is small for $\varepsilon_{\infty 3} \sim 1$ and large as $\varepsilon_{\infty 3} \gg 1$. The static coordinates are thus not explicitly represented in Eq. (7).

It is convenient to decouple the equations of motion using standard techniques that produce normal modes $x_\pm$ and normal mode frequencies $\Omega_\pm^2 = \bar{\Omega}_2^2 S_\pm^2(\theta) + \Omega_3^2 S_\mp^2(\theta) \pm g\sin(2\theta)/\sqrt{m_2 m_3}$, where $S_+(\theta) = \cos\theta$, $S_-(\theta) = \sin\theta$, and $\theta = (1/2)\tan^{-1}(2g/\sqrt{m_2 m_3}[\bar{\Omega}_2^2 - \Omega_3^2])$ is the mixing angle that determines the degree of hybridization between $x(\omega)$ and $Q_{01}(\omega)$. Here $g = -e^2/\sqrt{8d^3b_2^3}$ is a constant coupling strength that, along with the masses m_2 and m_3, sets the scale of mixing in the system, while the variable detuning $\bar{\Omega}_2^2 - \Omega_3^2$ between the modes' natural frequencies allows the system to transition through the point of maximal mixing where θ flips from $\pi/4$ to $-\pi/4$.

To visualize this transition, normal mode frequencies are superimposed on the spectra of Fig. 5 as the wave numbers $\nu_\pm = \Omega_\pm/2\pi c$ with $d = 1\,\text{cm}$ and $|g| = 2.0\times10^{-13}$ g/s^2. They demonstrate that the observable peaks of $|A_2(\omega)|$ are indeed located near the normal modes of the system even when the peaks have strange line shapes. Additionally, in

cases where one peak is difficult to discern, the hybridization model shows that one of the normal mode wave numbers $\nu_{\pm}$ has approached $\nu_3 = \Omega_3/hc$ such that the resonant line shape of the associated mode $x_{\pm}(\omega)$ has become buried by the parasitic signal from the substrate mode $Q_{00}(\omega)$ that couples directly with the tip.

Finally, we note that strong coupling has been achieved in the experimental systems with both SiO_2 and hBN substrates. This can be observed directly from the marked separation between the coupled resonances of the hBN substrate and can be inferred from an analysis of the difference of the squared hybrid frequencies at maximal mixing, $\Omega_+^2(\pi/4) - \Omega_-^2(\pi/4) = 2g/\sqrt{m_2 m_3}$. With the uncoupled SPhP masses $m_3 = 1.194 \times 10^{-46}$ g and 3.219×10^{-47} g in the SiO_2 and hBN substrates, respectively, and the nanorod's dipole mode mass $m_2 = 2.686 \times 10^{-36}$ g, the characteristic splitting constant $\sqrt{2|g|/\sqrt{m_2 m_3}}/2\pi c$ is equal to 793 cm^{-1} (SiO_2) and 1100 cm^{-1} (hBN), at least a factor of three larger than the linewidths $\gamma_3/2\pi c = 64.1$ cm^{-1} (SiO_2), 92.6 cm^{-1} (hBN), and $\gamma_2/2\pi c = 256$ cm^{-1} of the system.

Using a more traditional metric, one can see from the theoretical model that the hybridized resonances of both the SiO_2 and hBN systems are always split by at least the average of the uncoupled mode linewidths, such that $R(\theta) = 2|\Omega_+(\theta) - \Omega_-(\theta)|/(\gamma_2 + \gamma_3) > 1$ is satisfied for all mixing angles [71–73]. At maximal mixing ($\theta = \pi/4$), R is minimized and equal to 1.71 and 2.51, respectively. Additionally, with $\bar{\Omega}_2 = \Omega_3 = \Omega_0$ at maximal mixing, the splitting can be simplified via a power series to $\Omega_+(\pi/4) - \Omega_-(\pi/4) \approx g/\Omega_0\sqrt{m_2 m_3} = \sigma$, with σ the form of the coupling strength that appears in quantum-optical treatments of interacting cavities [74–76]. This simplification produces strong coupling ratios $R(\pi/4) \approx 2|\sigma|/(\gamma_2 + \gamma_3) = 1.71$ (SiO_2) and 2.48 (hBN), as well as values of 0.24 (SiO_2) and 0.31 (hBN) for the ultrastrong coupling condition $|\sigma|/\Omega_0$.

Experimental approximations of the strong and ultrastrong coupling conditions can also be recovered directly from the SINS data. However, as both substrates possess more than one SPhP that couples to the FP mode of the rod and none of the SPhP linewidths can be directly extracted from the signal, the coupling ratio R must be replaced by a similar ratio R' that contains only measurable quantities and accounts for the width of the Reststrahlen band. The most convenient form of the new ratio is $R'(\theta) = 2[|\Omega'_+(\theta) - \Omega'_-(\theta)| - \Delta]/[\gamma'_+(\theta) + \gamma'_-(\theta)]$, where $\Omega'_{\pm}$ are the measured hybrid frequencies, $\gamma'_{\pm}$ are the measured linewidths of the hybrid modes, and Δ is the Reststrahlen band width as reported in Fig. 4. At maximal mixing, $R'(\pi/4) = 1.35$ (SiO_2) and 2.10 (hBN), in good agreement with the theory. Finally, approximating the shared natural frequency of the SPhP and FP mode at maximal mixing, Ω'_0, to lie at the center of the Reststrahlen band, the ultrastrong coupling condition $|\sigma'|/\Omega'_0 \approx (\gamma_+ + \gamma_-)R'(\pi/4)/2\Omega'_0$ takes a value of 0.17 for either substrate material.

III. CONCLUSION

In conclusion, we report the observation of strong coupling between the $m = 1$ and 2 FP modes of $L = 0.7$–10.0 μm long gold nanorods and the SPhP modes of a polar crystal (SiO_2) and a van der Waals (hBN) substrate using SINS. The hybridization of the nanorod resonances with the substrate is made clear by the experiment, which leverages the unique IR sensitivity and spatial selectivity of SINS to characterize the anticrossing behavior of the hybrid FP-SPhP mode pairs as the FP modes are tuned in and out of resonance with the SPhPs. The coupling of the $m = 1$ mode is confirmed by a reduced-order model that describes in detail the individual interactions of the nanorod, substrate, and AFM tip to produce both a reconstruction of the SINS observable and a mechanical analogy that interprets the spectral features therein. Importantly, the theoretical model accounts for the interference of the substrate in the SINS signal and allows for the clear interpretation of SINS spectra that lack the clearly defined resonances observed in more familiar optical and electron-beam spectroscopies. This combined experimental and theoretical investigation of interacting IR resonances in a tunable nanoscopic system provides a blueprint for the design and fabrication of more tailored IR nanophotonic systems for use in future molecular sensing, cavity-controlled chemistry, and optical circuit applications.

IV. MATERIALS AND METHODS

Apparatus. The SINS setup consists of a synchrotron light source, KBr beamsplitter, rapid-scan FTIR system, atomic force microscope (AFM), and a mercury cadmium telluride (MCT) detector. The beamsplitter forms an asymmetric Michelson type interferometer with the rapid-scan FTIR as one arm and the AFM tip/sample as the other [46]. Light from the synchrotron, 3–13 μm wavelengths (3333–769 cm^{-1}) is focused onto the sample and platinum silicide AFM tip with a gold, 0.4 NA, parabolic mirror. Over multiple visits to the ALS we find that replicate samples yield quantitatively similar results indicating good reproducibility in the sample preparation and AFM tip conditions (see SM Fig. S5). The MCT detector records the recombined signal which is demodulated by a lock-in amplifier at the second harmonic. These interferograms are Fourier transformed, turning them into broadband spectral responses. The entirety of these experiments were collected with a spectral resolution of 32 cm^{-1}. A single point spectrum, which is actually an average of 256 individual scans, takes 90 s to acquire at this resolution. Since the setup is operating in the near to mid IR, the entire system is purged with N_2 to minimize atmospheric H_2O and CO_2 signatures.

Sample fabrication. The Au nanorod lengths are designed to be 0.5–4.0 (0.1 μm increments) and 1–10 (1 μm increments) μm with a constant height of 30 nm, a width of 100 nm, and a 50 nm radius of curvature at their ends. We expect these to exhibit both $m = 1$ and $m = 2$ FP mode resonances in the SINS energy range of 700–5000 cm^{-1} [24]. Au nanorods were patterned using electron beam lithography on (1) a 100 nm thermal SiO_2 film on a double side polished silicon wafer and (2) a 330 nm thick exfoliated flake of hexagonal boron nitride (hBN) on a double side polished silicon wafer. Additionally, a 10 μm × 10 μm × 30 nm Au structure was patterned, which provides a reference for the phase and magnitude information and serves to optimize the SINS MCT detector signal.

The substrate is cut to approximately 10 mm × 10 mm and mounted on a customized AFM sample holder with super glue.

ACKNOWLEDGMENTS

Work at the University of Notre Dame and at the University of Washington was supported by the U.S. Department of Energy (DOE), Office of Science, Office of Basic Energy Sciences (BES), Materials Sciences and Engineering Division under Award No. DE-SC0018169 (J.J.L., J.P.C.) and Award No. DE-SC0018040 (J.A.B., D.J.M.). P.D.R. and R.C. acknowledge support from NSF Grant No. DMR-1709275. Research at Lawrence Berkeley National Laboratory used resources of the Advanced Light Source, a U.S. DOE Office of Science User Facility under Contract No. DE-AC02-05CH11231. The authors acknowledge the nanofabrication was performed at the Center for Nanophase Materials Sciences, which is a DOE Office of Science User Facility. The authors would like to thank G. Gu at the University of Tennessee for exfoliating the hBN.

[1] D. Hagenmüller, J. Schachenmayer, C. Genet, T. W. Ebbesen, and G. Pupillo, ACS Photon. **6**, 1073 (2019).
[2] P. Pons-Valencia, F. J. Alfaro-Mozaz, M. M. Wiecha, V. Biolek, I. Dolado, S. Vélez, P. Li, P. Alonso-González, F. Casanova, L. E. Hueso *et al.*, Nat. Commun. **10**, 3242 (2019).
[3] M. Autore, L. Mester, M. Goikoetxea, and R. Hillenbrand, Nano Lett. **19**, 8066 (2019).
[4] Y. Zhong, S. D. Malagari, T. Hamilton, and D. M. Wasserman, J. Nanophoton. **9**, 093791 (2015).
[5] D. N. Basov, M. M. Fogler, and F. J. García de Abajo, Science **354**, aag1992 (2016).
[6] S. Tan, A. Argondizzo, J. Ren, L. Liu, J. Zhao, and H. Petek, Nat. Photon. **11**, 806 (2017).
[7] H. Lourenço-Martins and M. Kociak, Phys. Rev. X **7**, 041059 (2017).
[8] L. Wehmeier, D. Lang, Y. Liu, X. Zhang, S. Winnerl, L. M. Eng, and S. C. Kehr, Phys. Rev. B **100**, 035444 (2019).
[9] R. Qi, R. Wang, Y. Li, Y. Sun, S. Chen, B. Han, N. Li, Q. Zhang, X. Liu, D. Yu *et al.*, Nano Lett. **19**, 5070 (2019).
[10] M. Tamagnone, A. Ambrosio, K. Chaudhary, L. A. Jauregui, P. Kim, W. L. Wilson, and F. Capasso, Sci. Adv. **4**, eaat7189 (2018).
[11] J. Yang, Q. Sun, K. Ueno, X. Shi, T. Oshikiri, H. Misawa, and Q. Gong, Nat. Commun. **9**, 4858 (2018).
[12] Y. Wu, G. Li, and J. P. Camden, Chem. Rev. **118**, 2994 (2018).
[13] Y. Wu, J. Ordonez-Miranda, S. Gluchko, R. Anufriev, D. D. S. Meneses, L. Del Campo, S. Volz, and M. Nomura, Sci. Adv. **6**, eabb4461 (2020).
[14] A. M. Dubrovkin, B. Qiang, T. Salim, D. Nam, N. I. Zheludev, and Q. J. Wang, Nat. Commun. **11**, 1863 (2020).
[15] H. Hu, H. Duan, J. K. W. Yang, and Z. X. Shen, ACS Nano **6**, 10147 (2012).
[16] C. T. Ellis, J. G. Tischler, O. J. Glembocki, F. J. Bezares, A. J. Giles, R. Kasica, L. Shirey, J. C. Owrutsky, D. N. Chigrin, and J. D. Caldwell, Sci. Rep. **6**, 32959 (2016).
[17] F. Medeghini, A. Crut, M. Gandolfi, F. Rossella, P. Maioli, F. Vallée, F. Banfi, and N. Del Fatti, Nano Lett. **18**, 5159 (2018).
[18] M. Geisler, X. Cui, J. Wang, T. Rindzevicius, L. Gammelgaard, B. S. Jessen, P. A. D. Gonçalves, F. Todisco, P. Bøggild, A. Boisen *et al.*, ACS Photon. **6**, 994 (2019).
[19] A. B. Yankovich, B. Munkhbat, D. G. Baranov, J. Cuadra, E. Olsén, H. Lourenço-Martins, L. H. G. Tizei, M. Kociak, E. Olsson, and T. Shegai, Nano Lett. **19**, 8171 (2019).
[20] C. Cherqui, G. Li, J. A. Busche, S. C. Quillin, J. P. Camden, and D. J. Masiello, J. Phys. Chem. Lett. **9**, 504 (2018).
[21] A. Mancini, C. R. Gubbin, R. Berté, F. Martini, A. Politi, E. Cortés, Y. Li, S. De Liberato, and S. A. Maier, ACS Nano **14**, 8508 (2020).
[22] C. R. Gubbin, S. A. Maier, and S. De Liberato, Phys. Rev. B **95**, 035313 (2017).
[23] S. Castilla, I. Vangelidis, V.-V. Pusapati, J. Goldstein, M. Autore, T. Slipchenko, K. Rajendran, S. Kim, K. Watanabe, T. Taniguchi *et al.*, Nat. Commun. **11**, 4872 (2020).
[24] Y. Wu, Z. Hu, X.-T. Kong, J. C. Idrobo, A. G. Nixon, P. D. Rack, D. J. Masiello, and J. P. Camden, Phys. Rev. B **101**, 085409 (2020).
[25] G. W. Bryant, F. J. García de Abajo, and J. Aizpurua, Nano Lett. **8**, 631 (2008).
[26] F. Neubrech, D. Weber, R. Lovrincic, A. Pucci, M. Lopes, T. Toury, and M. L. d. L. Chapelle, Appl. Phys. Lett. **93**, 163105 (2008).
[27] T. Dattoma, M. Grande, R. Marani, G. Morea, V. Marrocco, and A. D'Orazio, Prog. Electromagn. Res. B **30**, 337 (2011).
[28] P. Zijlstra and M. Orrit, Rep. Prog. Phys. **74**, 106401 (2011).
[29] A. Crut, P. Maioli, N. Del Fatti, and F. Vallée, Chem. Soc. Rev. **43**, 3921 (2014).
[30] M. Klanjšek Gunde, Physica B: Condens. Matter **292**, 286 (2000).
[31] J. D. Caldwell, A. V. Kretinin, Y. Chen, V. Giannini, M. M. Fogler, Y. Francescato, C. T. Ellis, J. G. Tischler, C. R. Woods, A. J. Giles *et al.*, Nat. Commun. **5**, 5221 (2014).
[32] C. Huck, J. Vogt, T. Neuman, T. Nagao, R. Hillenbrand, J. Aizpurua, A. Pucci, and F. Neubrech, Opt. Express **24**, 25528 (2016).
[33] L. H. G. Tizei, V. Mkhitaryan, H. Lourenço-Martins, L. Scarabelli, K. Watanabe, T. Taniguchi, M. Tencé, J.-D. Blazit, X. Li, A. Gloter *et al.*, Nano Lett. **20**, 2973 (2020).
[34] N. C. Passler, C. R. Gubbin, T. G. Folland, I. Razdolski, D. S. Katzer, D. F. Storm, M. Wolf, S. De Liberato, J. D. Caldwell, and A. Paarmann, Nano Lett. **18**, 4285 (2018).
[35] A. Bouhelier, M. Beversluis, and L. Novotny, in *Quantum Electronics and Laser Science Conference* (Optical Society of America, Washington, DC, 2002).
[36] A. L. Lereu, A. Passian, and P. Dumas, Int. J. Nanosci. **9**, 488 (2012).
[37] A. García-Etxarri, I. Romero, F. J. García de Abajo, R. Hillenbrand, and J. Aizpurua, Phys. Rev. B **79**, 125439 (2009).
[38] K. Fritz and R. Hillenbrand, Philos. Trans. R. Soc. A **362**, 787 (2004).

[39] J. M. Atkin, S. Berweger, A. C. Jones, and M. B. Raschke, Adv. Phys. **61**, 745 (2012).
[40] B. Knoll and F. Keilmann, Nature (London) **399**, 134 (1999).
[41] R. C. Monreal, T. J. Antosiewicz, and S. P. Apell, J. Phys. Chem. Lett. **6**, 1847 (2015).
[42] R. C. Monreal, S. P. Apell, and T. J. Antosiewicz, Opt. Express **22**, 24994 (2014).
[43] R. C. Monreal, T. J. Antosiewicz, and S. Peter Apell, New J. Phys. **15**, 083044 (2013).
[44] N. Thakkar, N. P. Montoni, C. Cherqui, and D. J. Masiello, Phys. Rev. B **97**, 121403(R) (2018).
[45] J. Kim and K.-B. Song, Micron **38**, 409 (2007).
[46] H. A. Bechtel, E. A. Muller, R. L. Olmon, M. C. Martin, and M. B. Raschke, Proc. Natl. Acad. Sci. USA **111**, 7191 (2014).
[47] H. A. Bechtel, S. C. Johnson, O. Khatib, E. A. Muller, and M. B. Raschke, Surf. Sci. Rep. **75**, 100493 (2020).
[48] E. A. Muller, B. Pollard, H. A. Bechtel, R. Adato, D. Etezadi, H. Altug, and M. B. Raschke, ACS Photon. **5**, 3594 (2018).
[49] O. Khatib, H. A. Bechtel, M. C. Martin, M. B. Raschke, and G. L. Carr, ACS Photon. **5**, 2773 (2018).
[50] I. D. Barcelos, H. A. Bechtel, C. J. S. de Matos, D. A. Bahamon, B. Kaestner, F. C. B. Maia, and R. O. Freitas, Adv. Opt. Mater. **8**, 1901091 (2020).
[51] F. C. B. Maia, B. T. O'Callahan, A. R. Cadore, I. D. Barcelos, L. C. Campos, K. Watanabe, T. Taniguchi, C. Deneke, A. Belyanin, M. B. Raschke *et al.*, Nano Lett. **19**, 708 (2019).
[52] I. D. Barcelos, A. R. Cadore, A. B. Alencar, F. C. B. Maia, E. Mania, R. F. Oliveira, C. C. B. Bufon, A. Malachias, R. O. Freitas, R. L. Moreira *et al.*, ACS Photon. **5**, 1912 (2018).
[53] D. Schmidt, I. Kopf, and E. Bründermann, Laser Photon. Rev. **6**, 296 (2012).
[54] J. Duan, Y. Li, Y. Zhou, Y. Cheng, and J. Chen, Adv. Phys.: X **4**, 1593051 (2019).
[55] X. Chen, D. Hu, R. Mescall, G. You, D. N. Basov, Q. Dai, and M. Liu, Adv. Mater. **31**, 1804774 (2019).
[56] I. M. Pavlovetc, K. Aleshire, G. V. Hartland, and M. K. Kuno, Phys. Chem. Chem. Phys. **22**, 4313 (2020).
[57] See Supplemental Material at http://link.aps.org/supplemental/10.1103/PhysRevB.104.035412 for expanded theoretical derivations of the effective polarizability and oscillator models, as well as tabulated details of the experimental setups used to acquire the reported SINS spectra.
[58] K. Aleshire, I. M. Pavlovetc, R. Collette, X.-T. Kong, P. D. Rack, S. Zhang, D. J. Masiello, J. P. Camden, G. V. Hartland, and M. Kuno, Proc. Natl. Acad. Sci. USA **117**, 2288 (2020).
[59] R. Geick, C. H. Perry, and G. Rupprecht, Phys. Rev. **146**, 543 (1966).
[60] J. D. Caldwell, L. Lindsay, V. Giannini, I. Vurgaftman, T. L. Reinecke, S. A. Maier, and O. J. Glembocki, Nanophotonics **4**, 44 (2015).
[61] G. Jansen, J. Phys. A **33**, 1375 (2000).
[62] R. Hillenbrand, T. Taubner, and F. Keilmann, Nature (London) **418**, 159 (2002).
[63] R. Kitamura, L. Pilon, and M. Jonasz, Appl. Opt. **46**, 8118 (2007).
[64] J. Kischkat, S. Peters, B. Gruska, M. Semtsiv, M. Chashnikova, M. Klinkmüller, O. Fedosenko, S. Machulik, A. Aleksandrova, G. Monastyrskyi *et al.*, Appl. Opt. **51**, 6789 (2012).
[65] D. M. Hoffman, G. L. Doll, and P. C. Eklund, Phys. Rev. B **30**, 6051 (1984).
[66] J. W. Cleary, R. E. Peale, D. J. Shelton, G. D. Boreman, C. W. Smith, M. Ishigami, R. Soref, A. Drehman, and W. R. Buchwald, J. Opt. Soc. Am. B **27**, 730 (2010).
[67] S. Guo, N. Talebi, W. Sigle, R. Vogelgesang, G. Richter, M. Esmann, S. F. Becker, C. Lienau, and P. A. van Aken, Nano Lett. **16**, 6137 (2016).
[68] B. Schröder, T. Weber, S. V. Yalunin, T. Kiel, C. Matyssek, M. Sivis, S. Schäfer, F. von Cube, S. Irsen, K. Busch *et al.*, Phys. Rev. B **92**, 085411 (2015).
[69] S. V. Yalunin, B. Schröder, and C. Ropers, Phys. Rev. B **93**, 115408 (2016).
[70] A. Cvitkovic, N. Ocelic, and R. Hillenbrand, Opt. Express **15**, 8550 (2007).
[71] G. Khitrova, H. M. Gibbs, S. W. Koch, and A. Scherer, Nat. Phys. **2**, 81 (2006).
[72] L. Novotny, Am. J. Phys. **78**, 1199 (2010).
[73] D. S. Dovzhenko, S. V. Ryabchuk, Y. P. Rakovich, and I. R. Nabiev, Nanoscale **10**, 3589 (2018).
[74] K. C. Smith, Y. Chen, A. Majumdar, and D. J. Masiello, Phys. Rev. Appl. **13**, 044041 (2020).
[75] D. Yoo, F. de León-Pérez, M. Pelton, I.-H. Lee, D. A. Mohr, M. B. Raschke, J. D. Caldwell, L. Martín-Moreno, and S.-H. Oh, Nat. Photon. **15**, 125 (2021).
[76] A. F. Kockum, A. Miranowicz, S. De Liberato, S. Savasta, and F. Nori, Nat. Rev. Phys. **1**, 19 (2019).